# *Supplementary Material:* Radiometric Calibration from Faces in Images

Chen Li[1*] Stephen Lin[2] Kun Zhou[1] Katsushi Ikeuchi[2]
[1]State Key Lab of CAD&CG, Zhejiang University [2]Microsoft Research

## 1. Pseudo-albedo $\hat{A}$ for Single Pigment Density Change Identification

A key step to our approach is identifying the single pigment density change map $\mathcal{C}$ and we describe it in Sec. 5.1 in the main paper. We use the pseudo-albedo $\hat{A}$ by applying intrinsic image decomposition on the uncalibrated image $I$ instead of the skin albedo $A$. We show that the an accurate identification of $\mathcal{C}$ can be obtained only using $\hat{A}$.

Considering the nearby pixel pair $(p, q)$ satisfying the single pigment density change assumption, thus

$$A_q = \sigma^{\Delta} A_p, \tag{1}$$

where $\sigma$ is the relative absorbance vectors of the changing pigment and $\Delta$ is the density difference. Further assume the shading of $(p, q)$ are same, so by applying the camera response function $f$, we have

$$\begin{aligned} I_p &= f(A_p * D), &(2)\\ I_q &= f(\sigma^{\Delta} A_p * D), &(3)\end{aligned}$$

where $D$ is the diffuse shading of $(p, q)$.

Applying the intrinsic image decomposition on uncalibrated image $I$, we can decompose $I_p$ and $I_q$ into the pseudo-albedo $\hat{A}$ and pseudo-shading $\hat{D}$

$$\begin{aligned} I_p &= \hat{A}_p * \hat{D}, &(4)\\ I_q &= \hat{A}_q * \hat{D}. &(5)\end{aligned}$$

Combing Eq. (2),Eq. (3),Eq. (4), and Eq. (5), we have

$$\begin{aligned} \hat{A}_p * \hat{D} &= f(A_p * D), &(6)\\ \hat{A}_q * \hat{D} &= f(\sigma^{\Delta} A_p * D). &(7)\end{aligned}$$

Taking the ration of Eq. (6) and Eq. (7), we have

$$\frac{\hat{A}_p * \hat{D}}{\hat{A}_q * \hat{D}} = \frac{f(A_p * D)}{f(\sigma^{\Delta} A_p * D)}. \tag{8}$$

*This work was done while Chen Li was an intern at Microsoft Research.

Let considering a certain class, gamma function $f(x) = x^{\gamma}$, of the camera response function $f$, then

$$\begin{aligned} f(\sigma^{\Delta} A_p * D) &= (\sigma^{\Delta} A_p * D)^{\gamma}, &(9)\\ &= \sigma^{\Delta\cdot\gamma}(A_p * D)^{\gamma}, &(10)\\ &= \sigma^{\Delta\cdot\gamma} f(A_p * D). &(11)\\ & &(12)\end{aligned}$$

Combing Eq. (11) and Eq. (8) and eliminated the same factors, $\hat{D}$ and $f(A_p * D)$, appearing in both numerators and denominators, we have

$$\frac{\hat{A}_p}{\hat{A}_q} = \frac{1}{\sigma^{\Delta\cdot\gamma}}. \tag{13}$$

Denoting $\hat{\Delta} = \Delta \cdot \gamma$, we have

$$\hat{A}_q = \sigma^{\hat{\Delta}} \hat{A}_p. \tag{14}$$

Comparing Eq. (14) with Eq. (1), the single pigment density change property of pixel pair $(p, q)$ in skin albedo $A$ is preserved in its pseudo-albedo $\hat{A}$. As a result, the single pigment density change map $\mathcal{C}$ can be identified only using the pseudo-albedo $\hat{A}$, without known skin albedo $A$. Although the aforemention formula derivation only for a ceratin type of camera response function, our experiment results show $\mathcal{C}$ can be identified from $\hat{A}$ for any other camera response functions, not limited to a ceratin gamma functions.

## 2. Real Image Results

We present more real image results in this supplementary material. A quantitative error comparison over different cameras, namely DSLRs (*Canon EOS 5D*, *Nikon D5100*), MILCs (*SONY NEX-7*, *SONY a6000*), webcams (*Logitech Pro9000*, *ANC 152WS*), and mobile phone cameras (*iPhone 6 Plus*, *HUAWEI Mate8*), is given in Table 1. The results for each individual camera is shown from Fig. 1 to Fig. 8.

The results of EdgeCRF [2], GICRF [3] and RankCRF [1] depend on image content and their ability to find suitable local regions for their processing. Especially in outdoor images full of complex surfaces, there may be a number of erroneously detected regions

Table 1. Average radiometric calibration error for real images ($\times 10^2$).

| Cameras | EdgeCRF [2] | GICRF [3] | ISCRF [4] | RankCRF [1] | Ours w.o. shading | Ours |
|---|---|---|---|---|---|---|
| *Canon EOS 5D* | 11.3 | 16.7 | 5.91 | 4.47 | 5.5.61 | **3.29** |
| *Nikon D5100* | 20.5 | 15.9 | 11.2 | 11.0 | 5.69 | **4.03** |
| *SONY NEX-7* | 26.8 | 27.5 | 13.4 | 13.0 | 7.90 | **3.22** |
| *SONY $\alpha$6000* | 30.9 | 28.5 | 14.5 | 23.2 | 5.35 | **3.37** |
| *Logitech Pro9000* | 30.9 | 26.6 | 4.62 | 17.0 | 5.80 | **4.05** |
| *ANC 152WS* | 26.3 | 17.5 | 5.34 | 10.8 | 7.30 | **3.45** |
| *iPhone 6 Plus* | 16.0 | 22.0 | 5.19 | 4.11 | 4.70 | **2.71** |
| *HUAWEI Mate8* | 33.3 | 32.7 | 21.2 | 22.0 | 4.90 | **3.85** |

that do not actually satisfy the assumed properties and thus mislead the estimation. Although RankCRF [1] rely on the same scene radiance property as EdgeCRF [2], it performs a bit better than EdgeCRF [2] because the rank minimization is more robust at avoiding trivial solutions. GICRF [3] utilizes the locally planar region whose radiance have be approximated linearly. However, the number of these locally planar region is limited due to the non-uniform illumination, reflections, and complex textures in real world. ISCRF [4] works more effectively for cameras that generate more image noise, such as a webcam or a smartphone camera, and generally less well for higher quality images. In this experiment, ISCRF [4] happens to work well for some of the *Canon EOS 5D* images because of the blurred backgrounds due to depth-of-field and a higher ISO used for capturing indoor images with low illumination.

When a face is present, our approach can obtain relatively reliable estimates regardless of the other scene content, even if the face regions are not large, are captured under varying illumination, or are noisy. This is indicated by the average error statistics in Tab. 1. From these examples of typical images, it can be seen that faces are a useful source of radiometric calibration information that is effectively exploited by our technique.

## References

[1] J.-Y. Lee, Y. Matsushita, B. Shi, I. S. Kweon, and K. Ikeuchi. Radiometric calibration by rank minimization. *IEEE Transactions on Pattern Analysis and Machine Intelligence*, 35(1):144–156, Jan. 2013.

[2] S. Lin, J. Gu, S. Yamazaki, and H.-Y. Shum. Radiometric calibration from a single image. In *Computer Vision and Pattern Recognition, 2004. CVPR 2004. Proceedings of the 2004 IEEE Computer Society Conference on*, volume 2, pages II–938–II–945 Vol.2, June 2004.

[3] T.-T. Ng, S.-F. Chang, and M.-P. Tsui. Using geometry invariants for camera response function estimation. In *IEEE Computer Society Conference on Computer Vision and Pattern Recognition (CVPR)*, June 2007.

[4] J. Takamatsu and Y. Matsushita. Estimating camera response functions using probabilistic intensity similarity. In *Computer Vision and Pattern Recognition, 2008. CVPR 2008. IEEE Conference on*, pages 1–8, June 2008.

*Canon EOS 5D*

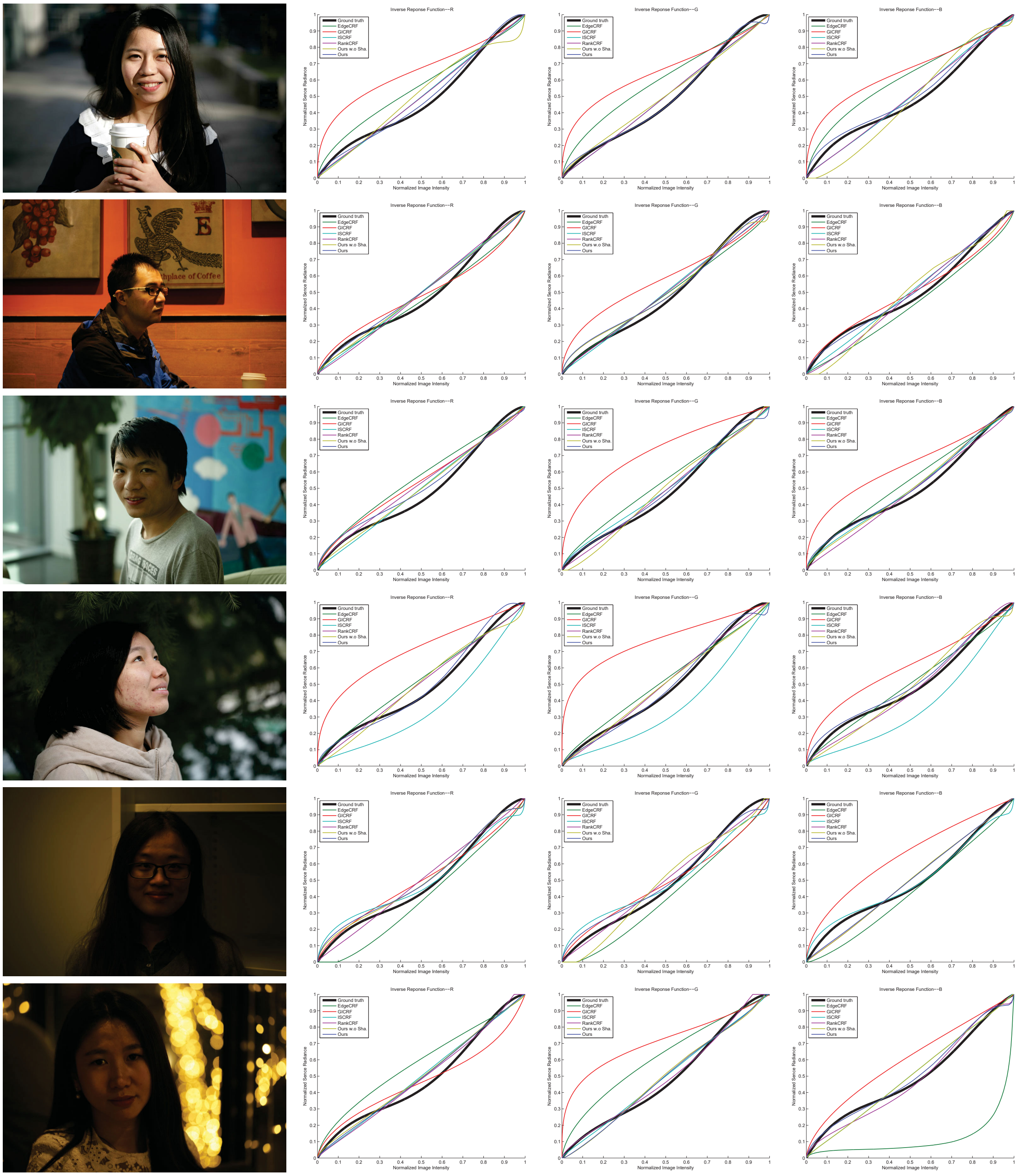


Figure 1. Real image results for *Canon EOS 5D*. Each raw shows a non-linear input image on the left, followed by the estimated inverse response functions for various methods as well as the ground truth for the R, G and B channels, respectively. Please zoom in for better viewing.

# *Nikon D5100*


Figure 2. Real image results for *Nikon D5100*. Each raw shows a non-linear input image on the left, followed by the estimated inverse response functions for various methods as well as the ground truth for the R, G and B channels, respectively. Please zoom in for better viewing.

# *SONY NEX-7*


Figure 3. Real image results for *SONY NEX-7*. Each raw shows a non-linear input image on the left, followed by the estimated inverse response functions for various methods as well as the ground truth for the R, G and B channels, respectively. Please zoom in for better viewing.

*SONY $\alpha$6000*

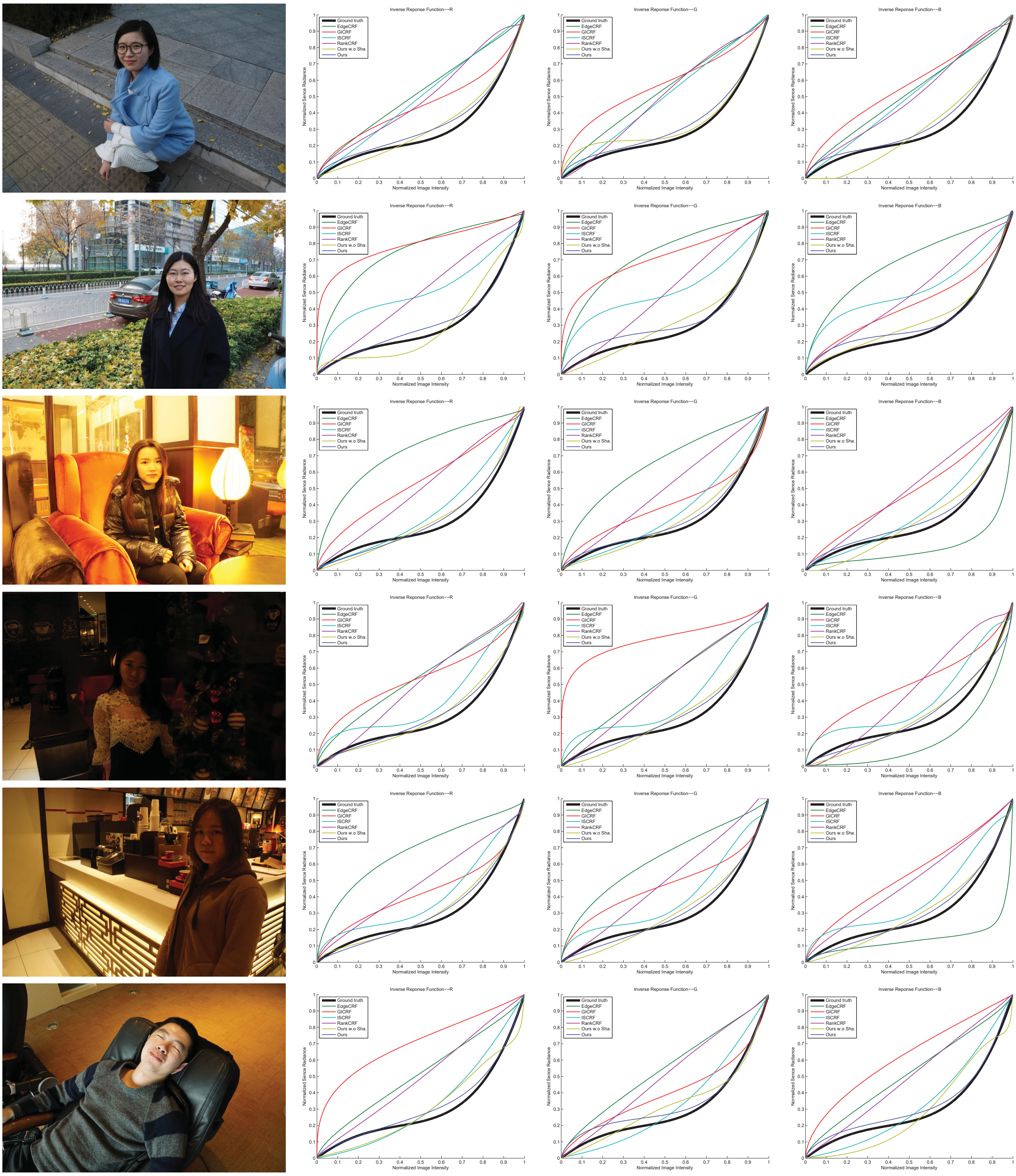


Figure 4. Real image results for *SONY $\alpha$6000*. Each raw shows a non-linear input image on the left, followed by the estimated inverse response functions for various methods as well as the ground truth for the R, G and B channels, respectively. Please zoom in for better viewing.

*Logitech Pro9000*

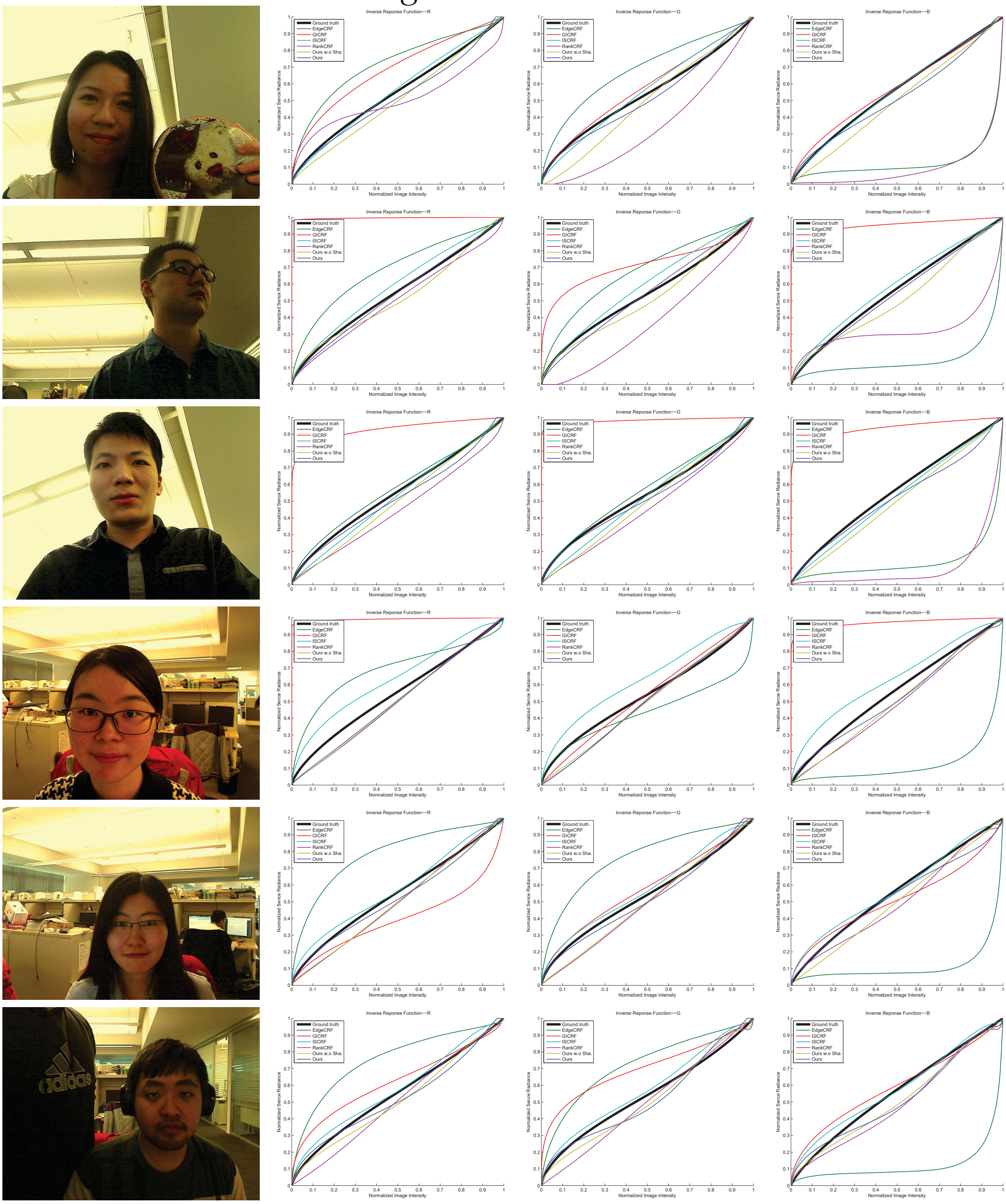


Figure 5. Real image results for *Logitech Pro9000*. Each raw shows a non-linear input image on the left, followed by the estimated inverse response functions for various methods as well as the ground truth for the R, G and B channels, respectively. Please zoom in for better viewing.

*ANC 152WS*

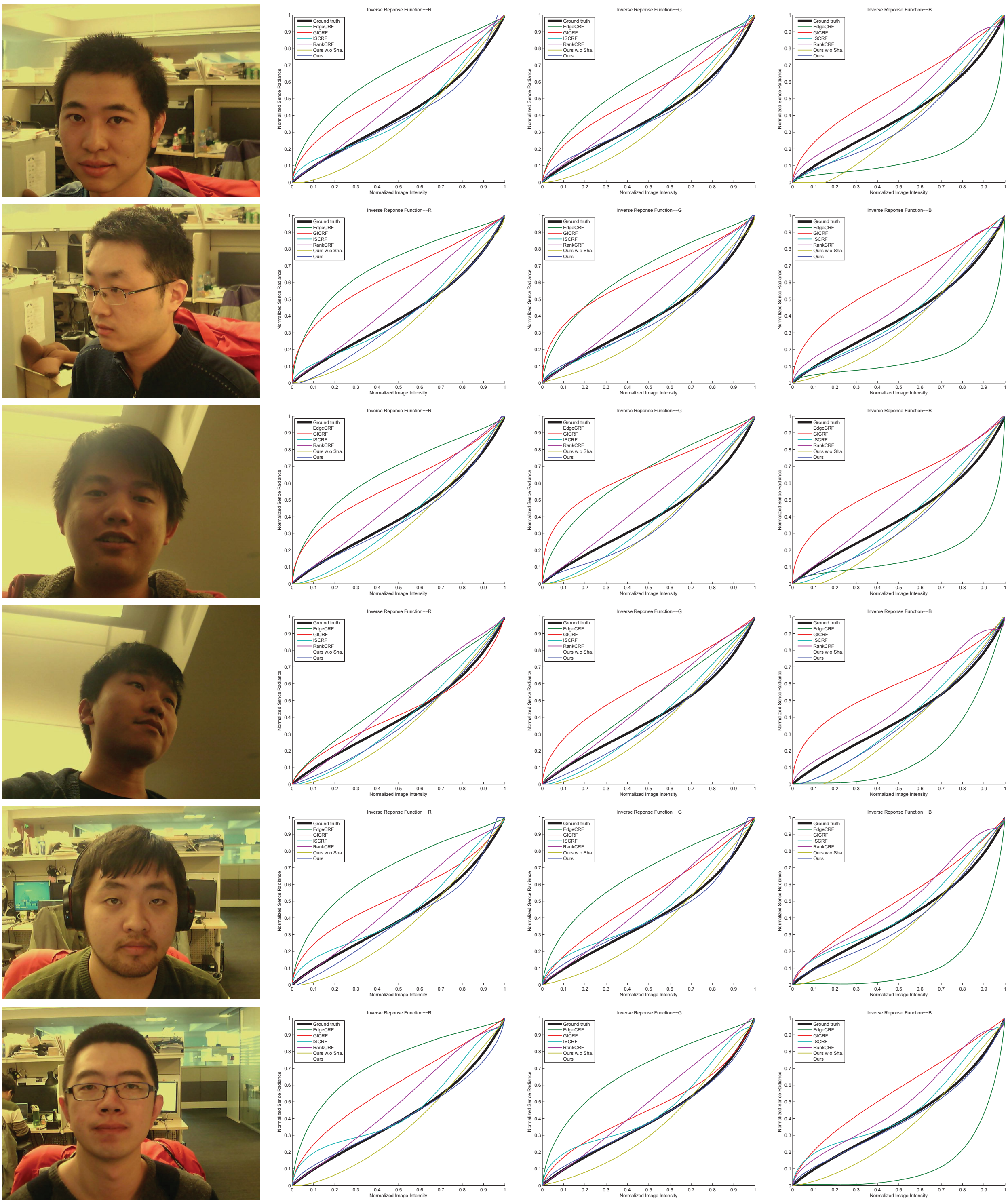


Figure 6. Real image results for *ANC 152WS*. Each raw shows a non-linear input image on the left, followed by the estimated inverse response functions for various methods as well as the ground truth for the R, G and B channels, respectively. Please zoom in for better viewing.

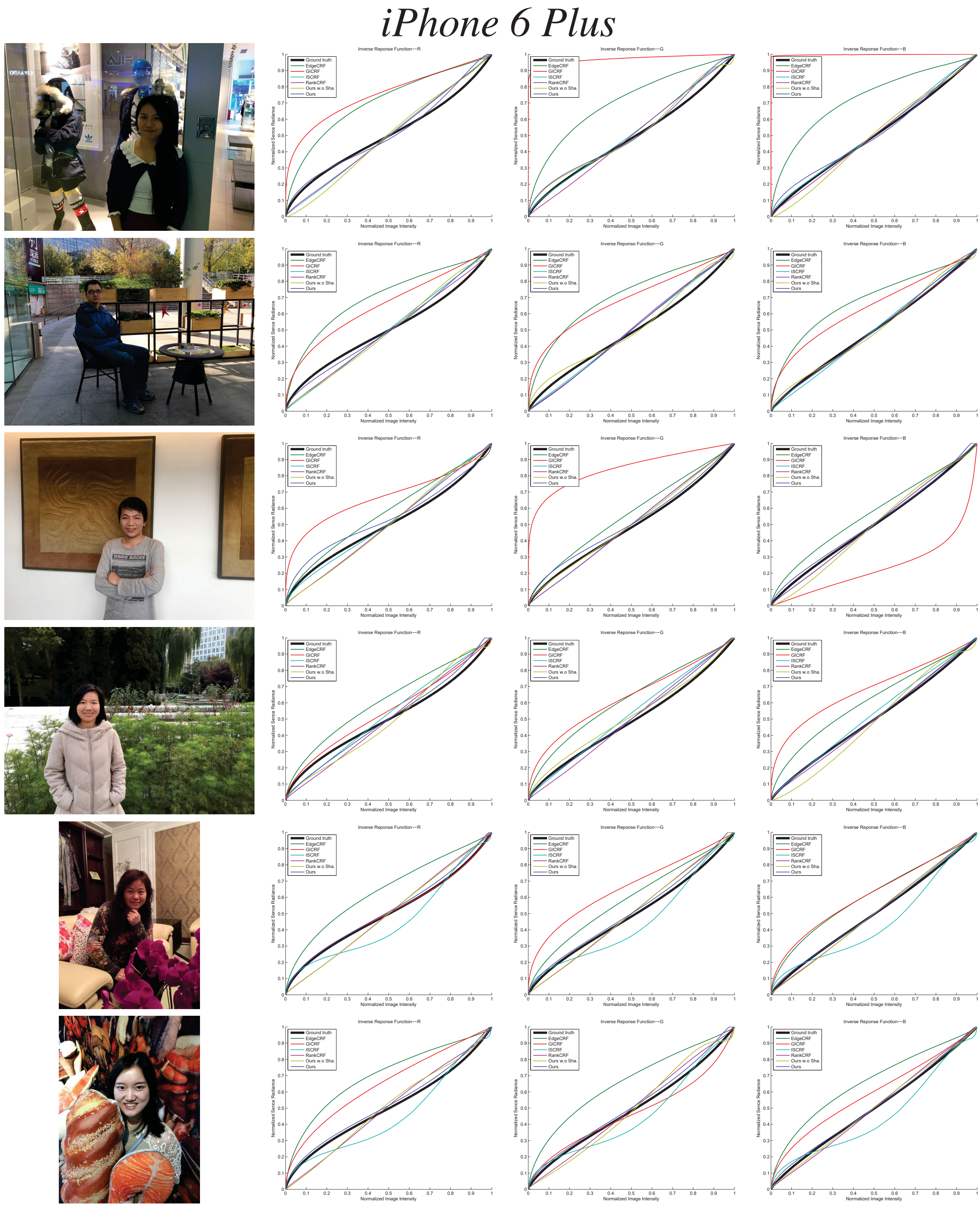


Figure 7. Real image results for *iPhone 6 Plus*. Each raw shows a non-linear input image on the left, followed by the estimated inverse response functions for various methods as well as the ground truth for the R, G and B channels, respectively. Please zoom in for better viewing.

# *HUAWEI Mate8*


Figure 8. Real image results for *HUAWEI Mate8*. Each raw shows a non-linear input image on the left, followed by the estimated inverse response functions for various methods as well as the ground truth for the R, G and B channels, respectively. Please zoom in for better viewing.